Influence of loading control on strain bursts and dislocation avalanches at the nanometer and micrometer scale

Yinan Cui, Giacomo Po, and Nasr Ghoniem

Phys. Rev. B **95**, 064103 — Published 8 February 2017

DOI: 10.1103/PhysRevB.95.064103

Influence of loading control on strain bursts and dislocation avalanches at the nano- and micrometer scale

Yinan Cui,* Giacomo Po, and Nasr Ghoniem
Mechanical and Aerospace Engineering Department, University of California, Los Angeles, 420 Westwood Plaza, Los Angeles CA, 90095

Through three-dimensional discrete dislocation dynamics simulations, we show that by tuning the mode of external loading, the collective dynamics of dislocations undergo a transition from driven avalanches under stress control to quasi-periodic oscillations under strain control. We directly correlate measured intermittent plastic events with internal dislocation activities and collective dynamics. Under different loading modes, the role of the weakest dislocation source and the defect population trend are significantly different. This finding raises new possibilities of controlling correlated dislocation activities, and obtaining low defect density in nano-structured devices by tuning external constraints. In addition, the effect of machine stiffness comes to light. The statistical analysis on the burst magnitude is revisited and carefully discussed. Self-organized criticality and scale-free statistics of strain bursts are obeyed under stress control. However, this behavior is shown to break down under strain control. Rapid stress drops under pure strain control force truncation of dislocations avalanches, leading to a dynamical transition to quasi-periodic oscillations.

I. INTRODUCTION

Recent investigations of plastic deformation of microscale materials reveal that the stress-strain relationship is not smooth, and that plastic strain is released in intermittent "bursts"[1–4]. Because of the generality of this behavior and similarity with many branches of statistical mechanics, this observation has quickly become a topic that continues to receive considerable experimental and theoretical attention[5–10]. Moreover, and from a purely technical point of view, such strain burst behavior makes it difficult to control microscale plastic forming, and may even induce catastrophic collapse of microdevices.

In order to explore the possibility of improving plastic deformation controllability, the underlying strain burst mechanism must be revealed, prompting the advancement of various views on its physical origins. For example, strain burst behavior is proposed to origininate from the collective and avalanche-like motion of dislocations due to long-range interactions[3]. On the other hand, the robust emissions of numerous pile-up dislocations in a particular area due to strain gradients[11], and the intermittent activation of dislocation sources[12–16] have also been proposed as viable mechanisms. An intriguing question is whether these different mechanisms are influenced by external constraints, and under which conditions one expects a burst mechanism transition? While some previous research discussed the external loading mode effect on the burst magnitude[12,17,18], a more systematic approach is still highly desirable. When one considers experimental studies, some extreme loading conditions are still difficult to be accessed, and may require development of future techniques. For example, it is difficult to distinguish the influence of the machine stiffness, the hysteresis response of the controlling system, and the deformation of the substrate etc. on the mechanism and statistical nature of strain bursts and dislocation avalanches. High-fidelity discrete dislocation dynamics (DDD) simulations can be viewed as complementary to experimental observations, and thus may allow accessibility to regimes not possible yet to present-day experimental techniques. DDD simulations are carried out here, which can give more detailed microstructure information with higher time resolution, and can systematically explore the dependency of the mechanical response on external loading control. In addition, investigation of the loading mode effect using the same initial dislocation configuration becomes possible. Our recent work[19] discussed the loading mode effect on the burst statistics. The present study will further demonstrate more plentiful insights into the physics of strain bursts tuned by loading mode control, including the role of weakest sources, activated slip system characters, dislocation density evolution, etc. Moreover, the simulation results bring to light the influence of the machine stiffness on the collective dynamics of dislocations and underlying mechanisms in nano- and micro-scale systems.

Recent realization that the strain burst size follows "scale-free" power law distribution has suggested its underlying connection with a wide array of vastly different physical systems, such as sand pile slides, snow avalanches, and geologic earthquakes[9,10,20]. Although much effort has been devoted to understanding these phenomena, methods of effective statistical analysis remain rather ambiguous, and are seldom discussed in detail. In this work, several key problems are described and carefully revisited, including identification of the strain burst event, selection of suitable physical quantities to describe power law distributions, and fitting procedures of the power law relationship.

The paper is organized as follows. In the next section, we provide a brief description of our DDD simulation method. Dislocation avalanche behavior and its underlying mechanisms under different loading modes are revealed. The influence of finite machine stiffness on the avalanche behavior and its correlated motion is then discussed. Afterwards, the statistics of strain bursts is fully explored, where we clarify mathematical aspects of statistical distributions. Finally, conclusions on the influence of load mode control and the results of statistical analysis are given.

II. SIMULATION SETUP

The investigative tool employed here is the MoDELib (Mechanics Of Defect Evolution Library) computer code[21], which has been described in detail in our previous papers[22–24]. In this model, arbitrary dislocation loops or curved segments are discretized into a succession of parametrized cubic splines. The complex topology of dislocations is updated every step to capture the processes of junction formation and destruction, and the occurrence of cross slip. Boundary conditions and image forces on dislocations are considered by seamless coupling of the original Parametric Dislocation Dynamics (PDDD) approach[22] with the finite element method based on the superposition principle of linear elasticity[24].

In this study, a series of DDD simulations of compression tests are performed on Cu single crystal micropillars with different diameters ranging from 1000 b to 3000 b ($\approx$ 300 nm- 1 μm), where b is the magnitude of the Burgers vector. For all investigated samples, the ratio of height h to diameter d is fixed to 3. Compression loading along the [001] direction is performed in order to achieve multi-slip conditions. Cu is approximated to be isotropic and the following properties are used: shear modulus $\mu = 48$ GPa, Poisson's ratio $\nu = 0.34$.

Initial equilibrium dislocation configurations are generated through relaxation of randomly distributed prismatic dipolar-loops without external loading until further dislocation activity is not noticeable. The advantage of using such

TABLE I: 0.2 % offset yield stresses by averaged 3D-DDD results

	Pure strain control	Pure stress control
d=1000 b (50 curves)	199 MPa	260 MPa
d=3000 b (20 curves)	101 MPa	147 MPa

initial dislocation configuration is discussed in our previous paper[16]. For each sample size, multiple different initial dislocation configurations are used in DDD simulations.

Three kinds of mechanical loading modes are applied. The first one is pure strain control (infinitely high machine stiffness), where the applied strain rate $\dot{\varepsilon}_0$ is equal to 960 s^{-1}. We noted that in our simulations under pure strain control, where the top surface moves according to a fixed displacement rate, it is possible that some dislocations pileup around the top and bottom surfaces. However, for an aspect ratio of 3 and a limited dislocation density in such small volume, most dislocations annihilate at the side surface instead of forming pileups around the top and bottom surfaces. The second is pure stress control (zero machine stiffness), where the applied loading rate $\dot{\sigma}_0$ is correspondingly $E\dot{\varepsilon}_0$, where E is the elastic modulus of the crystal. In previous DDD simulations work, stress-controlled compression loading is widely imposed via a cut-off plastic strain rate method[13,14]. Namely, if the calculated plastic strain rate is smaller than a specific value (such as 200 s^{-1}), the stress is discretely increased by some constant amount (for example 0.5 MPa). Else if the plastic strain rate is larger, the stress is kept constant. Obviously, this method requires determination of the critical plastic strain rate and the magnitude of the stress increment, which may influence the magnitude of dislocation avalanches. Recent high-resolution 3D-DDD simulations of stress-controlled compression test using a cut-off weighted dislocation velocity reveal an interesting crossover scaling behavior[25]. By contrast, the current work will shed light on understanding dislocation avalanches under pure stress controlled conditions.

In present-day experiments, perfect loading modes are almost impossible to be reached, especially for pure strain control. Thus, the third kind of loading mode is designed to simulate experimental strain-controlled modes by taking the finite machine stiffness effect into account. Experimentally, the external strain rate $\dot{\varepsilon}_0$ is applied through a combined open-loop and a closed-loop control system[19,26,27]. Here, a proportional dominated closed-loop control is simplified as a spring with finite machine stiffness K_p, which is connected in series with the micropillar. The actual stress rate $\dot{\sigma}$ felt by the crystal is then[19],

$$\dot{\sigma} = \frac{\alpha E}{1+\alpha}(\dot{\varepsilon}_0 - \dot{\varepsilon}^p) + \frac{\dot{\sigma}_0}{1+\alpha} \tag{1}$$

where α is the relative machine stiffness ($\alpha = K_p/K$). The effective sample stiffness $K = \frac{EA}{H}$, where A is the sample cross-sectional area, and H is its height. $\dot{\varepsilon}^p$ is the plastic strain rate of the crystal. $\dot{\sigma}_0$ is the open-loop stress rate, which is set to 0 here for finite α. According to Eq. 1, when α is equal to 0, the loading mode corresponds to pure stress control; when α is equal to ∞, it corresponds to pure strain control. More details about the correspondence between the simulation setup and actual experimental conditions are given in[19,28].

III. MICROSCALE PLASTICITY UNDER PURE STRESS AND PURE STRAIN CONTROL

A. Intermittent plasticity features

To obtain meaningful statical data, fifty and twenty initial dislocation configurations are studied under different loading modes for d=1000 b and d=3000 b, respectively. Parts of stress-strain curves obtained by 3D-DDD simulations are presented in Fig. 1. The increased scatter in smaller specimens and the size effect of the flow stress are naturally captured. Table I further gives the 0.2 % offset yield stresses corresponding to the averaged stress-strain curves for different cases (see Fig. 1). Even though the averaged yield stress under pure stress control is a little higher, the stress range is similar under both loading conditions (see Fig. 1).

Taking the case of a sample diameter d=1000 b as an example, one set of typical calculated stress-strain curves under pure strain control and pure stress control are plotted in Fig. 2 (a-b). Here, the results correspond to the same initial dislocation configurations to avoid any influence of the initial microstructure. It is clearly shown that under pure strain control and pure stress control, dislocation avalanches are manifested as sharply serrated and steplike character of the stress-strain curve, respectively. This is consistent with previous observations[3]. Moreover, under pure stress control, the stress almost monotonically increases. However, under pure strain control, it is possible that a strain burst occurs at a lower stress level compared with that for a previous strain burst event. This will be explained in the next subsection.

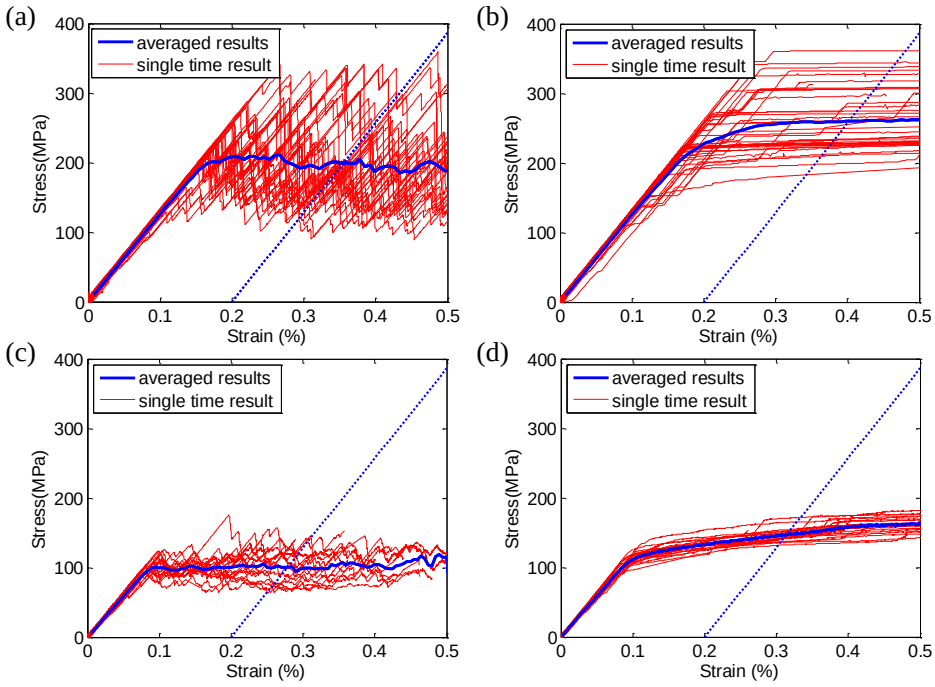

FIG. 1: Stress evolution and 0.2 % offset yield stresses corresponding to the averaged stress-strain curves for (a) d=1000 b, pure strain control; (b) d=1000 b, pure stress control; (c) d=3000 b, pure strain control; (d) d=3000 b, pure stress control

Figure 2 also presents the corresponding evolution of the plastic dissipated energy rate $\dot{E}_d$, which reflects the extent of plastic deformation. Previous 2D-DDD generally assume that the dissipated energy is proportional to the square of the dislocation velocity[1], and neglect the variation of the dislocation length during deformation. This is inherent in 2D simulations, since dislocations are assumed to be infinitely long. In the current work, the dissipated energy rate is calculated as follows,

$$\dot{E}_d = \int \boldsymbol{\sigma}_{ij}\dot{\boldsymbol{\varepsilon}}^p_{ij} dV = \sum_{i=1}^{N_{dis}} \boldsymbol{f}_i^{PK}\boldsymbol{v}_i dl \tag{2}$$

where $\boldsymbol{\sigma}$ is the calculated total stress tensor, $\boldsymbol{\varepsilon}^p$ is the plastic strain tensor, the summation convention is employed with respect to repeated subscripts (i, j). N_{dis} is the total number of the dislocation segments, $\boldsymbol{f}_i^{PK}$ is the Peach-Koehler force on the ith dislocation segment, and $\boldsymbol{v}_i$ is the corresponding segment velocity. According to Fig. 2, it is interesting to note that under pure strain control, the dissipated energy rate evolves in a similar fashion to crackling noise, and that each peak stage of the dissipated energy rate exactly corresponds to the stress drop stage in the stress-strain curve (see Fig. 2(a)). Under pure stress control mode, however, the dissipated energy rate evolves in a more continuous way, and its magnitude shows good correspondence with each stress step stage (see Fig. 2(b)).

B. Dislocation mechanisms

These distinct burst features under different loading modes are found to be associated with starkly different dislocation mechanisms. Deep in the sub-micron regime (such as d=1000 b), each strain burst under pure strain control is dominated by the one-by-one activation and deactivation of single arm sources[19]. After a dislocation source is activated (see Fig. 3 (a)), the accompanied plastic strain leads to a rapid decrease in the stress level (see Fig. 2), which further induces deactivation of all sources, and thus terminates the strain burst. During one strain burst event, if some sources that are weaker than previously activated ones form, the next strain burst may occur at a lower stress level, such as indicated by points d and f in Fig. 2 (a) and Fig. 3. On the other hand, if no weaker sources form, the following strain burst can only occur at a higher stress level (see point h in Fig. 2(a) and Fig. 3). This implies

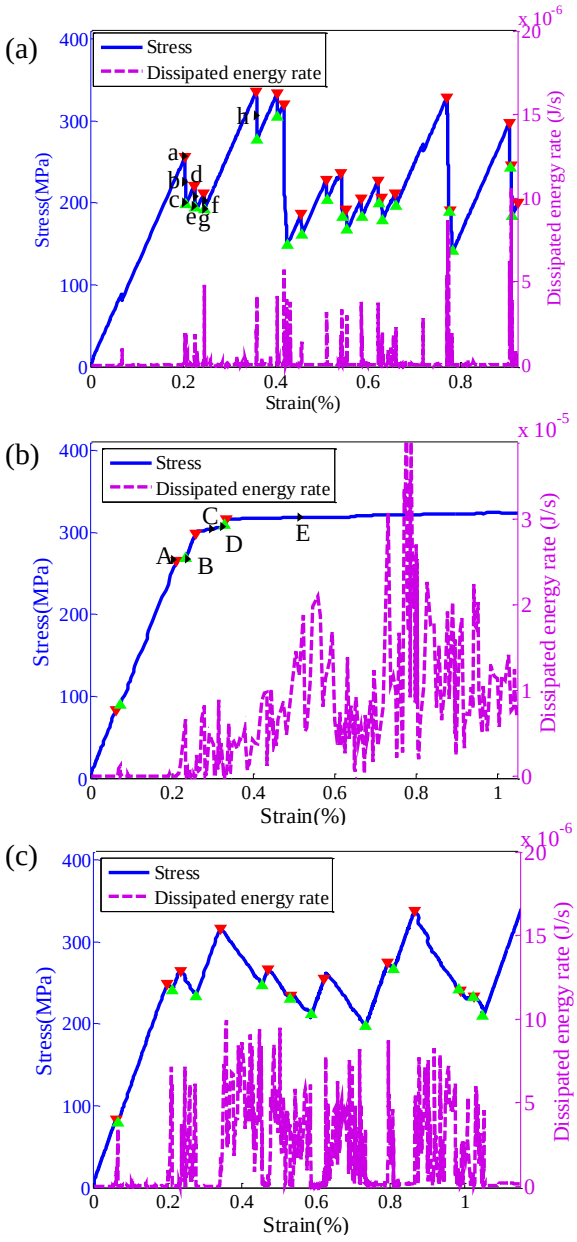

FIG. 2: Evolution of stress and dissipated energy rate for a pillar with diameter 1000 b under (a) pure strain control, (b) pure stress control and (c) finite machine stiffness ($\alpha = 0.5$). Here, the red points and green points are used to indicate recognized start and finish times of an avalanche event, respectively

that under pure strain control, the required stress level to trigger a strain burst is controlled by the strength of the weakest source[29].

By contrast, each dislocation avalanche under pure stress control is induced by the correlated motion of dislocations. If one activated source leads to the formation of a weaker source, it can be activated immediately, because the stress level keeps almost constant during each dislocation avalanche event, and would be high enough to activate this weak source (see Fig. 3E). Thus, different from pure strain control, the new generated weaker sources cannot make the subsequent dislocation avalanche occur at a lower stress level. Instead, the new generated weaker sources can only contribute to increasing the magnitude of the current dislocation avalanche event under pure stress control. Therefore, the dislocation avalanche magnitude can reach a very high value under pure stress control, which further leads to the near absence of strain hardening or to a low strain hardening rate (see Fig. 1 (b) and (d)).

Note that with an increase in the external size, it is possible that several dislocation sources simultaneously operate during one burst event under pure strain control. For example, in Fig. 4 (e), the arrows indicate the bowing out

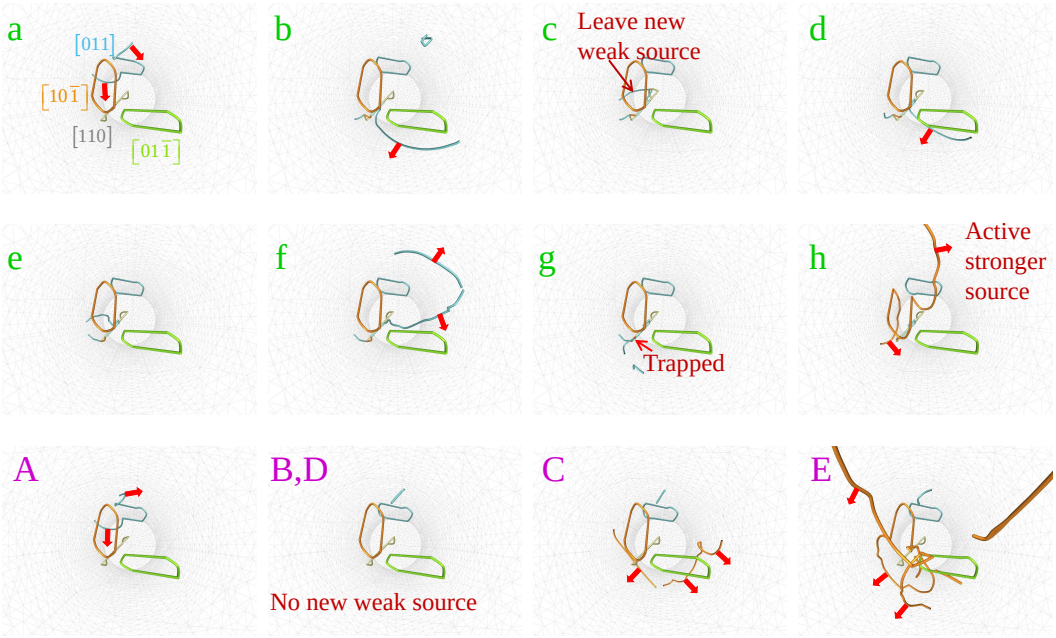

FIG. 3: Snapshots of dislocation configurations corresponding to the letters marked in Fig. 2 (from top view). Here, different colors in the figure are used to represent different Burgers vectors as indicated in (a). The thick arrows indicate the bowing out direction of activated dislocation sources.

TABLE II: Difference of avalanche/burst behaviors under pure strain control and pure stress control

	Pure strain control	*Pure stress control*
Burst mechanism	Intermittent activation of sources	Highly correlated dislocation motion
Activated sources in one event	Less	More
New generated weak sources	May determine next burst stress	Only increase current burst size
Dislocation density evolution	Apt to keep stable or decrease	Higher possibility to increase
Application implications	A mechanism to anneal out defects	A mechanism to accumulate defects

direction of activated sources. Three sources are simultaneously active in pillar with d=3000 b. However, the number of simultaneously activated sources is still much lower than that under pure stress control, as shown in Fig. 4(g). Here, Fig. 4 (e) and (g) correspond to the same initial dislocation configuration and strain level.

In addition, for submicron crystals, numerous dislocations glide out of the crystal. Analyzing these annihilated dislocations can help in understanding the activated dislocation character during the whole deformation process. As shown in Fig. 4(b) and (f), under pure strain control, most of the annihilated dislocations correspond to the same Burgers vector and concentrate in a relative narrow region, which implies that the plastic strain is apt to concentrate in the highly active slip system, and exhibit a relatively localized deformation mode. By way of contrast, under pure stress control, multiple slip systems are simultaneously activated, leading to a more homogeneous deformation mode, as shown in Fig. 4(d) and (h).

The analysis above implies that under pure stress control, the simultaneous activation of the first activated sources and the subsequently activated weaker sources increases the possibility of dislocation interaction, which may lead to more significant dislocation multiplication. This is also verified by the simulation result of the dislocation density evolution, as shown in Fig. 5. In contrast, under pure strain control, it is possible to realize the individual activation and destruction of the dislocation sources without introducing significant dislocation interaction and multiplication. Thus, the dislocation density can keep constant (see Fig. 5) or even completely vanish at such small scales (starvation mechanism). This discovery has current practical implications on regulating the defect density and controlling the dislocation fate at submicron scales by designing the loading conditions. Moreover, this also explains why mechanical annealing is mostly observed under stain-controlled micropillar compression tests[31], and strain-controlled low amplitude cyclic loading tests[32,33]. For clarity, the difference of avalanche behaviors under pure strain and pure stress control discussed above are further summarized in Table II.

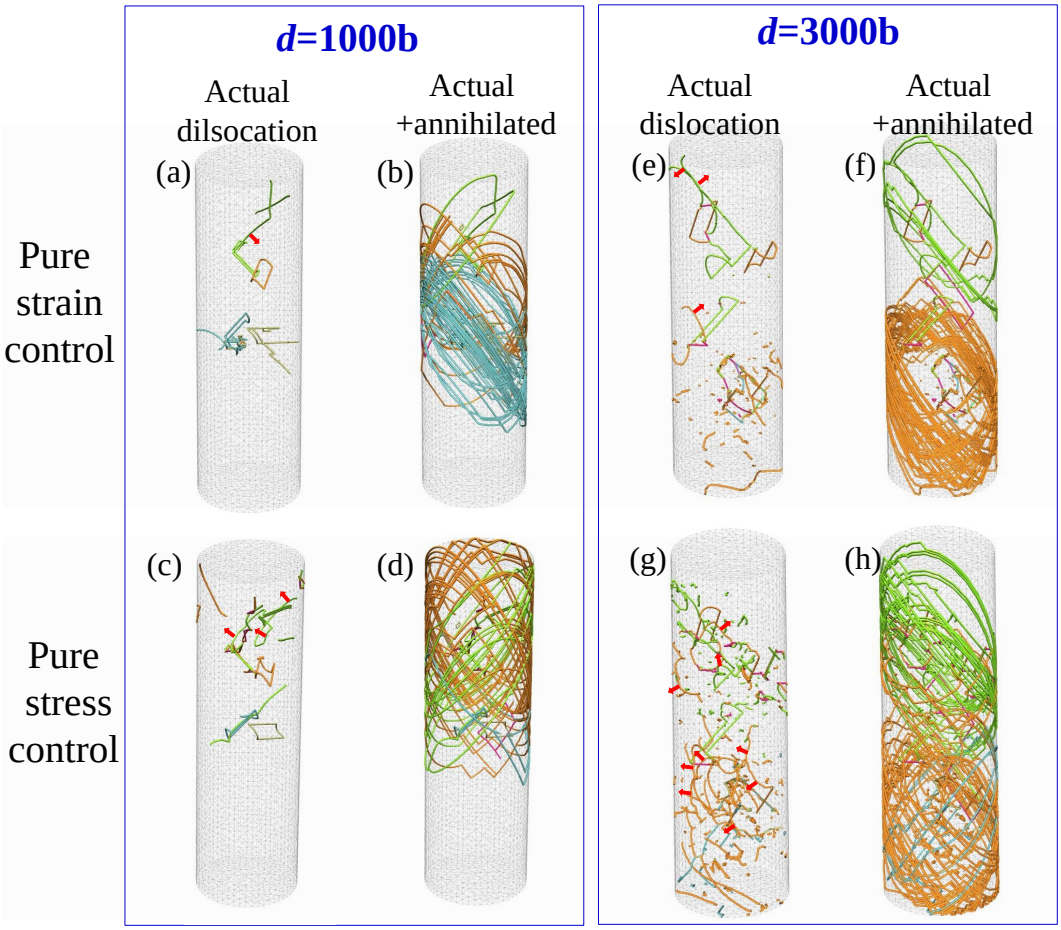

FIG. 4: Snapshots of dislocation configurations. (a-d) correspond to a pillar with d=1000 b at strain 1%, (a-b) under pure strain control, and (c-d) under pure stress control; (e-h) correspond to a pillar with d=3000 b at strain 0.5%, (e-f) under pure strain control, and (g-h) under pure stress control. 'Actual+ annihilated' means actual dislocation, together with the dislocations that have been annihilated from the free surface during all previous deformation stages. Different colors are used to represent dislocations with different Burgers vector. The thick arrows in (a, e, c, g) indicate the bowing out direction of activated dislocation sources. In (g), some small dislocation debris loops are left due to multiple cross slip[30].

IV. INFLUENCE OF FINITE MACHINE STIFFNESS

As discussed earlier, it is difficult to realize the pure strain and stress control loading mode in present-day experiments. We wish now to describe how the finite machine stiffness of the loading apparatus affects the strain burst behavior, as this relates directly to experimental results. To illustrate this issue and keep consistency with the discussion in the previous section, simulation results corresponding to the same size and same initial microstructure as that presented in Fig. 2 (a-b) are described below. As shown in Fig. 2 (c), the stress-strain curve corresponding to a finite machine stiffness using $\alpha = K_p/K = 0.5$ is very similar to the experimental results[18], which exhibit serrated yielding with longer decaying stages as compared with the results of pure strain control.

For the finite machine stiffness case shown in Fig. 6 (a), the difference between the target applied strain and the pillar strain reflects the deformation of the spring, namely the control system error. Even though the target applied strain rate keeps constant during the whole deformation stage, the actual strain of the pillar exhibits pronounced jerky character, as shown in Fig. 6 (a). This directly manifests itself through the sudden change of the pillar height. It is also the reason why the pillar height change rate is widely used as a signal to characterize the burst event during strain-controlled experiments[10,20,34]. Moreover, each jerky pillar strain event is induced by extensive motion of dislocations, which corresponds to intermittent high plastic strain rate, as shown in Fig. 6 (b). This plastic strain

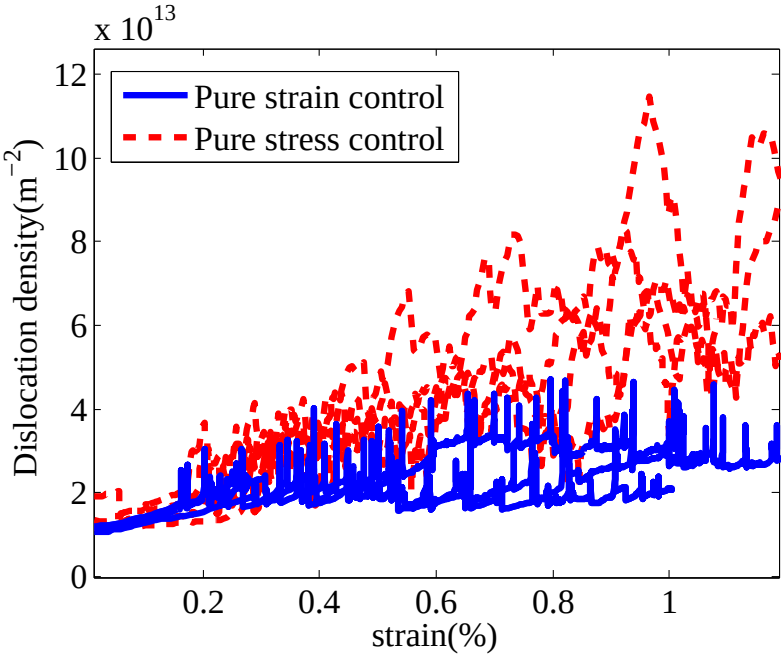

FIG. 5: Comparison of dislocation density evolution under pure strain control and pure stress control for three pillars with diameter 1000 b and different initial dislocation configurations

rate can reach a higher value than the target applied strain rate (corresponds to the continuous background value). At this time, the indenter cannot fully catch the motion of the pillar, and the pillar is actually subjected to unloading, which is reflected in the evolution curve of the applied stress rate ($\dot{\sigma}$ in Eq. 1) in Fig. 6 (b). According to Eq. 1, the slope of the stress-strain curve during the unloading stage is influenced by the machine stiffness, and approximately proportional to $\alpha/(1+\alpha) = K_p/(K+K_p)$. In Fig. 7, the simulation results using different machine stiffness are further given. It is clearly indicated that if the machine stiffness is high (such as $\alpha = K_p/K = 1$), the proportional closed-loop control system seems too sensitive, and a complete unloading may quickly occur. Such unloading phenomenon is also widely observed in micropillar compression experiments[35]. In contrast, if the machine stiffness is low (such as $\alpha = K_p/K = 0.1$), the stress-strain curve becomes similar to that under pure stress control.

Moreover, the evolution of the dissipated energy rate for a finite machine stiffness in Fig. 2 (c) also indicates the correspondence between intermittent high dissipated energy rate and the stress drop stage in the stress-strain curve. Compared with pure strain control, the dissipated energy rate evolves in a more correlated fashion, which is similar to that under pure stress control. This suggests that the finite machine stiffness promotes correlated dislocation motion due to the slower stress drop.

V. BURST AND AVALANCHE STATISTICS

We discuss here the statistical properties of strain bursts and the relationship between load mode control and system dynamics. Before proceeding with the analysis, however, we clarify several key issues pertaining to the statistical properties of strain bursts in nano- and micro-scale systems.

A. Statistical analysis of strain bursts

The first key question is how to identify a single strain burst event in a stochastic time series resulting from correlated dislocation motion. The widely used method is to set a threshold and identify an event if the magnitude of the continuing part of the signal is greater than the threshold[6,36]. For pillar compression tests, the rate of change of the micropillar height, V_h (corresponding to the strain rate of the pillar $V_h = \dot{\varepsilon}H$), is widely used as a criterion. One strain burst event is individualized by two time constants through the following relations[10,20,34],

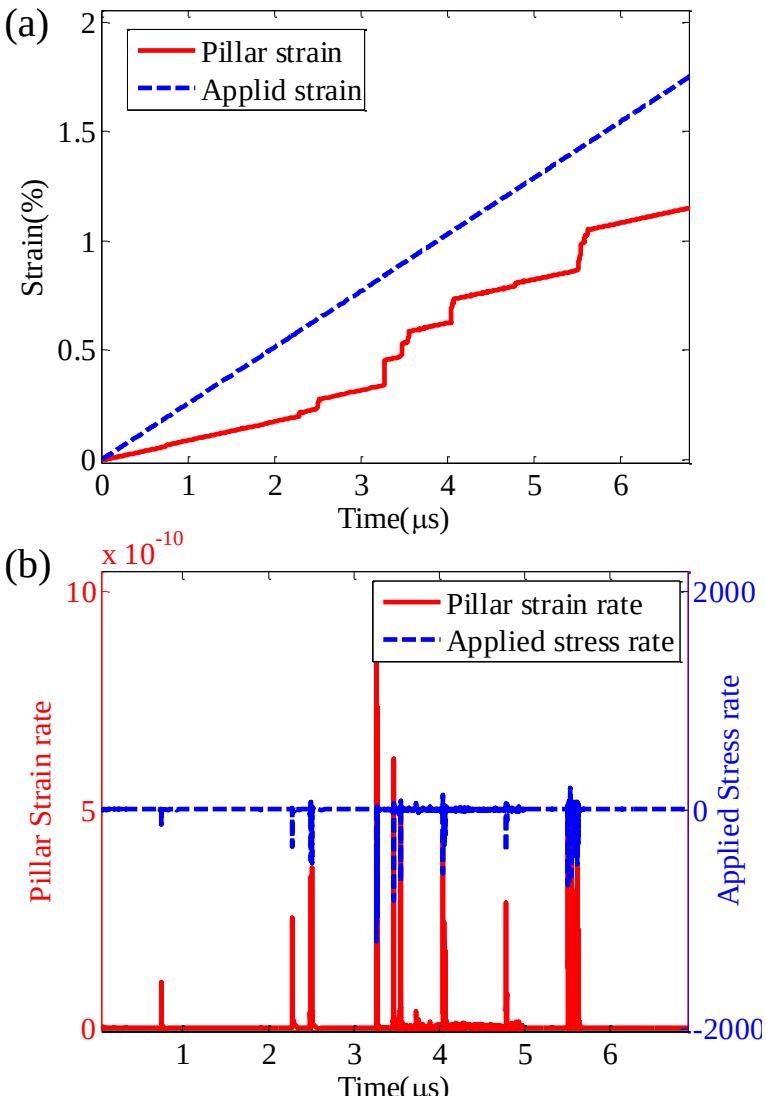

FIG. 6: (a) Time evolution of pillar strain and target applied strain; (b) Time evolution of the strain rate and the applied stress rate of the pillar during simulations in the case of $\alpha = 0.5$

$$\begin{aligned} V_h(t_s) = V_h(t_e) = V_{thr}, \\ V_h(t) > V_{thr} \quad \text{for} \quad t_s < t < t_e \end{aligned} \tag{3}$$

where V_{thr} is the threshold height rate of change, t_s is used to determine the starting time of the event, and t_e is used to determine the ending time of the event. However, this criterion is not suitable to distinguish strain burst under pure strain control because at this time, the height rate of change of the micropillar keeps constant during the whole deformation stage. Considering that the plastic strain rate is the direct magnification of the underlying dislocation activity, it is used as the criterion quantity similar to Eq. 3, as discussed in detail in our previous work (see Fig. S2 in[19]). The threshold plastic strain rate is taken as a few times of the applied strain rate to avoid numerical noise. This is also the method used in the present work. In addition, the dissipated energy rate is also a good measure of the plastic deformation extent, and can also be used to distinguish burst events, similar to acoustic emission experiments,

$$\begin{aligned} \dot{E}_d(t_s) = \dot{E}_d(t_e) = \dot{E}_{dthr}, \\ \dot{E}_d(t) > \dot{E}_{dthr} \quad \text{for} \quad t_s < t < t_e \end{aligned} \tag{4}$$

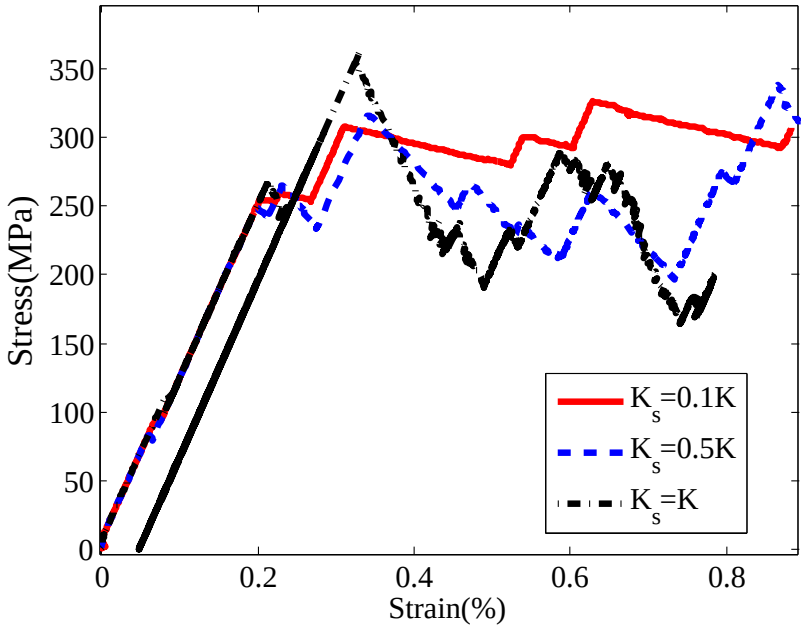

FIG. 7: Typical stress-strain curves under experimental strain control using a variety of machine stiffnesses

where $\dot{E}_{dthr}$ is the maximum dissipated energy rate during the elastic loading stage. One problem is the estimation of $\dot{E}_{dthr}$ because it is not as direct as the threshold plastic strain rate. Thus, different values of $\dot{E}_{dthr}$ should be used to check its influence on the statistical analysis. Fig. 2 (a-c) show some typical results of the recognized strain burst events using $\dot{E}_{dthr} = 5 \times 10^{-7} Js^{-1}$. Here, the red downward and green upward triangles correspond to t_s and t_e, respectively. This clearly shows that the strain burst event exactly corresponds to the stress drop stages and stress plateau regimes under strain control and stress control, respectively.

Similar to the diversity of choosing a criterion to quantitatively distinguish a single burst event, we have several possibilities to describe the power law distribution of strain burst events. Various parameters have been used, as summarized in Table III, to quantify the statistics of strain bursts. The plastic strain increment produced by a dislocation avalanche has been selected in references[3,17], because the related results can give information to develop stochastic crystal plasticity models[37]. Other investigations used the displacement magnitude and stress drop magnitude corresponding to each burst[2,38], because they are easy to be experimentally measured. In addition, the acoustic energy has also been used, based on the acoustic emission experimental technic[1,6]. Even though previous researchers proposed various models to relate acoustic emission to dislocation motion[39,40], the widely accepted parameters are the amplitude of acoustic emission, which is proportional to the plastic strain rate, and the acoustic energy, which corresponds to the plastic dissipated energy[1,41]. Moreover, other probability distributions have also been investigated, such as the dislocation velocity according to 2D-DDD, the time integral of segment-length weighted dislocation velocity[25], the burst duration time[20], the dependence of burst size on the stress level[7], etc. Till now, it is not clear which scaling variable is better suited to describe the scaling law of strain bursts, recognizing that all these parameters are manifestations of collective dislocation dynamics. The calculated scaling exponents for these descriptive parameters are summarized in Table III. In addition, if the power law distribution exists for these mentioned parameters, how do they correlate with each other? A rough estimation is given in Appendix B for uniaxial loading tests.

The present 3D-DDD simulations are free of many obscuring assumptions, and are detailed enough so as to allow recording different statistical metrics. These include the plastic strain increment $\Delta\varepsilon^p = \int_{t_s}^{t_e} \dot{\varepsilon}^p dt = \varepsilon^p(t_e) - \varepsilon^p(t_s)$, the displacement increment $\Delta U = \Delta\varepsilon^p H$, stress drop under strain control $\Delta\sigma = \sigma(t_e) - \sigma(t_s)$, the energy dissipation for complex 3D dislocation microstructure (see Eq. 2) $\Delta E_d = \int_{t_s}^{t_e} \dot{E}_d dt = E_d(t_e) - E_d(t_s)$, and burst duration $\Delta t_d = t_e - t_s$. This makes it possible to carry out a systematic study on these quantities using the same set of data. Note that the displacement increment ΔU is not set to $U(t_e) - U(t_s)$, because the displacement increment corresponding to one strain burst event is too small under pure strain control, which cannot represent the corresponding rapid plastic deformation. Considering that the stress drop quantity has no physical meaning under pure stress control, the statistical investigation on $\Delta\sigma$ is not carried out. Thus, in the next section, the statistical analysis is carried out on the burst displacement ΔU, burst dissipated energy ΔE_d, and burst duration Δt_d.

Before proceeding with the statistical analysis, another key question must be answered: what is the best method to

TABLE III: Power law distributions used to describe strain avalanche statistics. where $\Delta\varepsilon^p$ is plastic strain increment, ΔU is displacement increment, $\Delta\sigma$ is stress drop magnitude, V is absolute dislocation velocity, s is the time integration of segment-length weighted dislocation velocity, ΔW_{ac} is acoustic energy, ΔE_d is dissipated energy, H represents hight, b represents Burgers vector magnitude, U_c is constant, s^* represents characteristic strain burst size, k controls the sharpness of the crossover between the two power laws, ΔE_{dc} is the characteristic avalanche dissipated energy magnitude, "Exp"is the abbreviation of "experiment"

Scaling parameter	Probability distribution	Exponent	Investigation method and material	Loading control mode
$\Delta\varepsilon^p$	$\propto (\Delta\varepsilon^p)^{-m_{ep}} exp(-(\Delta\varepsilon^p/\Delta\varepsilon_0^p)^2)$	$m_{ep} = 1.5$	3D-DDD, FCC[3]	Stress/Strain
		1.5	Theory[17]	Stress/Strain
	$\propto (\Delta\varepsilon^p)^{-m_{ep}}$	1.6	DDD, FCC[42]	Strain
ΔU	$\propto (\Delta U)^{-m_U}$	$m_U = 1.5 \sim 1.6$	Exp, FCC[2]	Hybrid loading
		$1.34 \sim 1.76$	Exp, BCC[43]	Stress
		$1.47 \sim 1.67$	Exp, FCC[7]	Stress
		1.5	3D-DDD, Theory, FCC[19]	Stress
	$\propto (\Delta U/b)^{-m_U} exp(-\Delta U/U_c)$	1.5	Exp, FCC, BCC[44]	Strain
	$\propto (\Delta U)^{-m_U} exp(-A(\tau_c - \tau)^2)$	1.5	Exp, FCC, BCC[10,18]	Strain/Stress
$\Delta\sigma$	$\propto (\Delta\sigma)^{-m_\sigma}$	$m_\sigma = 1 \sim 1.5$	Exp, Alloy[45]	Strain
		$1.2 \sim 1.6$	Molecular dynamics, FCC[46,47]	Strain
V	$\propto V^{-m_V}$	$m_V = 3$	2D-DDD, FCC[9]	Stress
s	$\propto \frac{s^{-m_1}}{e^{s^b}} \left[1 + (\frac{s}{s^*})^{(m_1-m_2)k}\right]^{1/k}$	$m_1 = 1.52, m_2 = 1.75$	3D-DDD, FCC[25]	Hybrid loading
ΔW_{ac}	$\propto (\Delta W_{ac})^{-m_W}$	$m_W = 1.6$	Exp, Ice[1]	Creep
		$1.8, W_{ac} = V^2$	2D-DDD[1]	
		1.5 ± 0.1	Exp, HCP[48]	Strain
		1.54 ± 0.08 for Cu 2 ± 0.05 for Al	Exp[49]	Strain control Cyclic tension
ΔE_d	$\propto (\Delta E_d)^{-m_E} exp(-(\Delta E_d/\Delta E_{dc})^2)$	m_E =1.5	Theory[50]	Stress

analyze the power law distribution according to limited data sets? While the complementary cumulative distribution function (CCDF) is widely used, it is interesting to understand its advantage compared with the probability distribution function (PDF). In obtaining statistical data, the results are dependent on binning of the random variable. Thus, we need to address the difference between using linear binning and logarithmic binning for PDF. Finally, the mathematical procedure of fitting a power law to the data is relevant. These detailed issues are presented in the Appendix A.

B. Scaling exponent

Figure 8 presents results of statistical analysis of 3-D DDD simulation data. To obtain the maximum resolution of limited simulation data (due to computational limitations), the CCDF is used here. The probability of the burst size under pure stress control will be first discussed. As shown in Fig. 8 (a), ΔU under pure stress control mode exhibit scale-free power law size distribution, spanning several orders of magnitude. The power law exponent for its corresponding probability density is 1.5, consistent with previous work ($1.35 \sim 1.67$)[2,3,7,51]. In Fig. 8 (b), the magnitude distribution of burst dissipated energy follows a power law relation with an exponent close to 1.5, which is close to the value for acoustic energy and dissipated energy listed in Table III. Fig. 8 (c) further shows the temporal statistics, clearly showing a power law distribution of burst durations, irrespective of system size. This suggests that the system is critical in the plastic instability state. The existence of power law behavior among these different parameters has also been observed in the microfracturing phenomenon[52].

In contrast, the CCDF of ΔU under pure strain control, shown in Fig. 8 (a), seems to not obey a well-defined scaling behavior. At the same time, most of the data concentrate within one order of magnitude. A similar breakdown of the power law distribution under pure strain control is also observed for the burst dissipated energy, as indicated by Fig. 8 (b). Even though the distribution of burst duration seems to follow some kind of power law, the frequency-size range is very narrow (spanning less than one order of magnitude), as shown in Fig. 8 (c). This is because the rapid stress

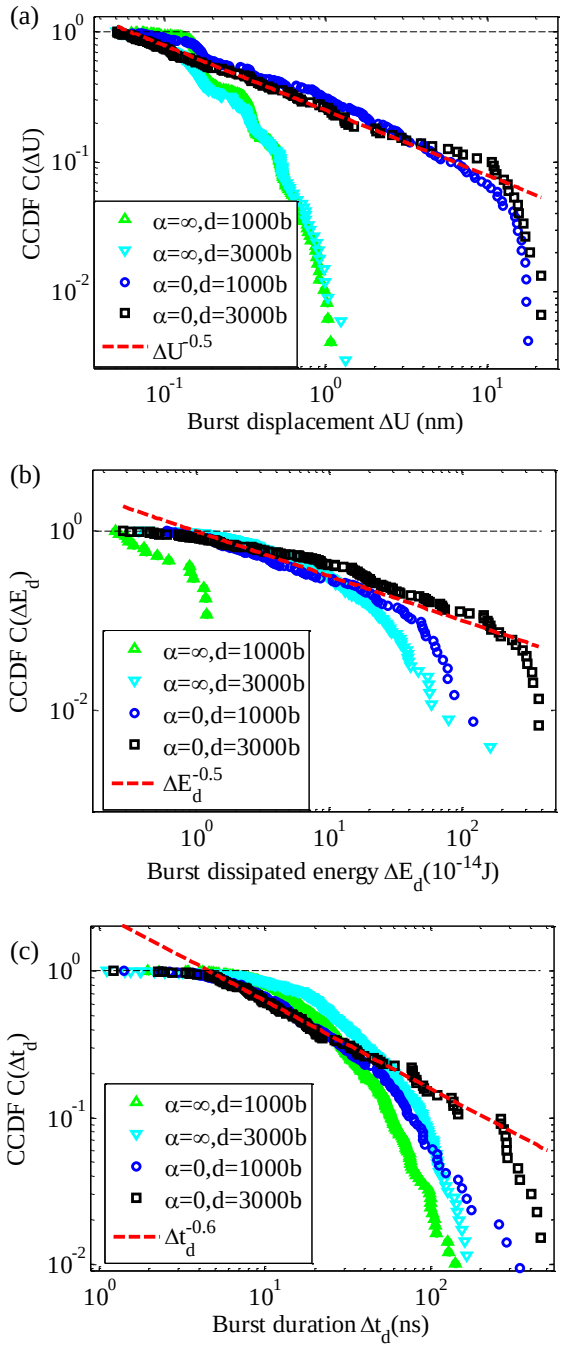

FIG. 8: CCDF of burst displacement (a)[19], burst dissipated energy (b), and burst duration(c) under pure strain control and stress control for pillars with different diameters

drop under pure strain control forces a truncation of the avalanche size, which makes it difficult to self-organize and exhibit scale-free power law distribution. Our recent work suggests that under pure strain control, the rate of change of the driving force is comparable to that of the internal relaxation rate; a condition which violates the Self-Organized Criticality (SOC) assumption. Although based on different physical arguments, a transition between different types of criticality was also observed in a prototypical elastic spin model of deformation recently proposed by[53].

As discussed in detail in our recent study[19], pure strain control loading mode leads to a dynamical transition of the dislocation system to quasi-periodic oscillations. Quasi-periodic strain bursts manifests themselves through the smoothed plastic strain rate, as clearly shown in Fig. 2 in[19]. If there is only a single dislocation source in a sample,

where cross-slip events are rare (e.g. at low temperature). Intermittent activation and deactivation of the dislocation source will lead to well-defined periodicity in the external stress so as to keep up with strain bursts. However, the the intrinsic scatter induced by random cross slip or complex dislocation interactions leads to the destruction of perfect periodicity. For complex dislocation configuration, the power spectral density (PSD) of stress evolution to some extent exhibits Brownian noise character superimposed on quasi-periodic oscillations under pure strain control. Namely, according to the time evolution of stress values under pure strain control, the PSD $P(f)$ and the frequency f has a power law relation, $P(f) \approx f^{-k}, k = 2.3 \pm 0.3$ as indicated in Fig. 9. This relationship is calculated by fitting each simulation results independently using the peak points values of the PSD. It implies the existence of temporal self-similarity of stress drop with a fractal dimension 2.3 ± 0.3.

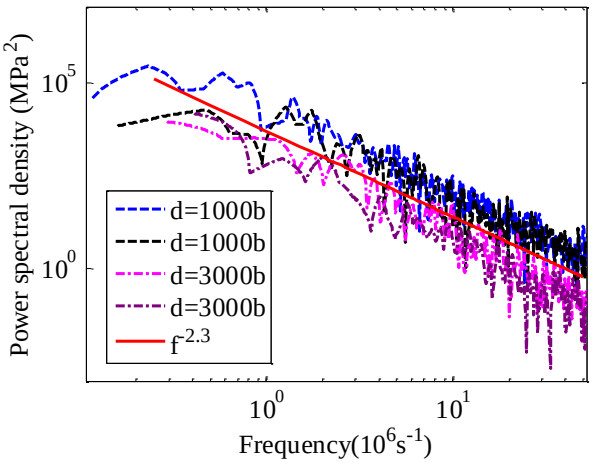

FIG. 9: Power spectral density of stress evolution results with logarithmic binning under pure strain control obtained by DDD simulations, showing quasi-periodic oscillations superimposed with approximate Brownian noise. For each size, two typical results are given

VI. SUMMARY AND CONCLUSIONS

Systematic 3D-DDD simulations have been carried out to provide new insights into the influence of external mechanical load control on the behavior of strain bursts and dislocation avalanches at the nano- and micro-scales. Simulation results showed that when the external constraint changes from pure strain control to pure stress control, the burst mechanism is altered from intermittent operation of dislocation sources to highly correlated dislocation motion. Additionally, the plastic deformation morphology tends to change from being localized to a more homogeneous mode. Newly-generated weak dislocation sources during one burst event may determine the stress level of subsequent bursts under pure strain control, but only increases the current avalanche magnitude under pure stress control. The more correlated dislocation motion under pure stress control promotes more significant dislocation interactions and multiplication. Therefore, strain control seems to be more suitable as a technique to mechanically anneal out defects in order to obtain defect-free nano- and micro-crystals.

The machine stiffness effect, which was not considered in earlier studies, has been shown to have significant impact on the physics of nano- and micro-scale plasticity. The simulations presented here successfully capture the different extents of serrated yielding characters tuned by machine stiffness, and the occasional unloading behavior with relatively high machine stiffness. These findings agree well with experimental results. At the same time, it also explains why the rate of change of sample height can be used as a signal to characterize the burst event during strain-controlled experiments.

Statistical analysis of intermittent plasticity has been considered, and several key problems have been discussed, including the distinction of burst events, and a description of the fitting procedure for the power law relation. Finally, statistical analysis has been carried out on different descriptive parameters, showing their inter-relationships. In addition, the comparison between the statistical analysis of burst magnitude under different loading modes suggests that while SOC and scale-free statistics of strain bursts are obeyed under stress control, this behavior breaks down under strain control. This work not only sheds light on the reliable control of plastic deformation in micro- and nano devices, but also deepens our understanding of the universality of avalanche statistics.

ACKNOWLEDGEMENTS

This material is based upon work supported by the U.S. Department of Energy, Office of Science, Office of Fusion Energy Sciences, under Award Number DE-FG02-03ER54708, and the US Air Force Office of Scientific Research (AFOSR), under award number FA9550-16-1-0444. We would like to thank Professor Stefanos Papanikolaou (West Virginia University) for inspiring comments and discussions.

APPENDIX A. FITTING PROCEDURE FOR THE POWER LAW DISTRIBUTION

Assuming that there is a perfect power law probability density function for a random variable, s,

$$P(s) = as^k, (s_{min} < s < s_{max}) \tag{5}$$

where a is a constant value and can be determined by normalization, $\int_{s_{min}}^{s_{max}} P(s)ds = 1$, s_{min} and s_{max} are the minmum and maximum values of s. Its cumulative distribution function $A(s)$ and complementary cumulative distribution function (CCDF) $C(s)$ can be calculated as follows,

$$\begin{aligned} A(s) &= \int_{s_{min}}^{s} P(s)ds = \frac{a}{k+1}(s^{k+1} - s_{min}^{k+1}) \\ C(s) &= \int_{s}^{s_{max}} P(s)ds = \frac{a}{k+1}(s_{max}^{k+1} - s^{k+1}) \\ &\approx -\frac{a}{k+1}s^{k+1}, \quad \text{if } s_{max} \gg 1, and\ k < -1 \end{aligned} \tag{6}$$

For the statistical analysis of the avalanche size, the power law exponent k approximately ranges from -1 to -3. Eq. 6 illustrates that when the exponent $k < -1$ and s_{min} is small, s_{min}^{k+1} is not negliable, so the cumulative distribution function A(s) cannot be approximated as a power law function of s. Therefore, cumulative distribution function is not used for determining the power law exponent. In contrast, for a power law probability density function with exponent k, Eq. 6 indicates that its CCDF approximately exhibits power law form with exponent $k+1$. However, it is noteworthy that when s is on the same order of magnitude of s_{max}, the CCDF may deviate from a good power law form, because s^{k+1} is close to s_{max}^{k+1}. This means that the deviation of the power law form in the CCDF cannot be used to determine the maximum cut-off value of the power law distribution. Furthermore, there may be significant errors when determining the power law exponent using this range of data (approximately, $s_{max}/5 < s < s_{max}$). This discussion is important for accurate investigation of the power law distribution using the CCDF.

Compared with the probability density function, the CCDF is preferred because there is no need to introduce any artificial binning size[10]. This advantage is especially attractive when the total data number N is limited. For example, there are one set of data $s_1, s_2, ...s_i, ..., s_N$. It is easy to sort them so that $s_1 \leqslant s_2 \leqslant ... \leqslant s_i \leqslant ... \leqslant s_N$. Thus, $C(s_i) = (N-i)/N$, here i is the sequence number of s_i among the data. Therefore, every data can contribute to the CCDF, leading to the maximum resolution. In contrast, if N is not large enough, accurate statistical analysis using the probability density function requires careful choice of the bin width.

For linear binning with a bin width ds^0, the sum of the probability function over each linear binning $P_{\text{linear}}(s)$ is,

$$\begin{aligned} P_{\text{linear}}(s) &= \int_{s-ds^0/2}^{s+ds^0/2} P(s)ds \\ &= \frac{a}{k+1}\left((s+\frac{ds^0}{2})^{k+1} - (s-\frac{ds^0}{2})^{k+1}\right) \approx a \cdot ds^0 \cdot s^k \end{aligned} \tag{7}$$

where $P_{\text{linear}}(s)$ approximately exhibits power law by using Taylor expansion of Eq. 7. This means that the smaller the linear bin width ds^0, the more accurate the calculated power law exponent. However, the limited data make it difficult to decrease ds^0 to a very small value. In addition, linear binning induces dense data around the high value region in a logarithmic plot. Thus, logarithmic binning, defined as exponentially increasing the width, is suggested. Similarly, one can calculate the integration of the probability density function over each logarithmic binning $P_{log}(s)$,

$$P_{\log}(s) = \int_{e^{lns-ds^*/2}}^{e^{lns+ds^*/2}} P(s)ds$$
$$= \frac{a}{k+1} s^{k+1} \left(e^{(k+1)ds^*/2} - e^{-(k+1)ds^*/2} \right) \tag{8}$$

Eq. 8 shows that $P_{log}(s)$ exactly exhibits power law irrespective of the logarithmic binning width. Note that the power law exponent of $P_{log}(s)$ is $k+1$ instead of k. The discussion above illustrates that the probability density function with logarithmic binning is a good way to investigate power law distribution when the number of data points is relatively large. However, when the data is limited and spans many orders of magnitude, the best way to determine the power law exponent is by using the CCDF, while the maximum cut-off value should be determined by using the probability density function with logarithmic binning.

To accurately calculate the power law exponent, one uses a least-squares fit or a maximum likelihood estimator. This is discussed in detail in Clauset et al.'s work[54]. They concluded that the maximum likelihood estimator is a better choice. The basic calculation process can be simply described as follows. Given a set of data (observations) $s_1, s_2, ...s_i, ..., s_N$ $(s_{min} < s_i < s_{max})$ and a statistical probability density model $P(s) = as^k, (s_{min} < s < s_{max})$, the unknown exponent k is evaluated so that the probability (likelihood) for the observation is greatest,

$$k = \arg\max_k \left[k \left(\sum_{i=1}^{N} \ln s_i \right) + N \ln a \right] \tag{9}$$

The lower cut-off s_{min} can be determined according to Bauke's and Zhang et al.'s method[51,55]. A sequence of exponents k is evaluated according to Eq. 9 by using different lower cut-offs s_{min}. If the calculated k is plotted against s_{min}, s_{min} is close to the starting point of the plateau regimes of this curve. More accurately, the s_{min} is chosen when the Kolmogorov-Smirnov statistical parameter, which is used to describe the maximum distance between the fitting value and actual data, is a minimum[51].

APPENDIX B. ROUGH ESTIMATION OF THE RELATION BETWEEN DIFFERENT POWER LAW DISTRIBUTIONS

A rough estimation of the relationship between power law distributions using different observables is given as follows for uniaxial loading tests. Here, the plastic strain increment serves as a reference quantity, and its power law exponent is expressed as m_{ep}. The displacement increment can be calculated as $\Delta U = \Delta\varepsilon^p H$. Due to the linear correlation between $\Delta\varepsilon^p$ and ΔU, their statistical trend should be the same. As expected, similar power law exponents are observed for ΔU and $\Delta\varepsilon^p$, as shown in Table III. The stress drop under strain control is $\Delta\sigma = E(\Delta\varepsilon - \Delta\varepsilon^p)$. Considering that during each burst event, the plastic strain rate is much higher than the applied strain rate $(\Delta\varepsilon^p \gg \Delta\varepsilon)$, $\Delta\sigma \approx -E\Delta\varepsilon^p$. Therefore, the power law exponent m_{ep} is close to m_σ in Table III. With respect to the dislocation velocity v, according to Orowan equation,

$$\dot{\varepsilon}^p \propto \rho_m b v \tag{10}$$

where ρ_m is the mobile dislocation density, which is generally an implicit function of plastic strain. Only if $\rho_m \Delta t_d$ changes little during deformation, the statistical trends of $\Delta\varepsilon^p$ and dislocation velocity are similar. Here, Δt_d is burst duration.

The burst dissipated energy ΔE_d can be estimated as follows,

$$\dot{E}_d = \sum_{i=1}^{N_{dis}} \boldsymbol{f}_i^{PK} \boldsymbol{v}_i dl = \sum_{i=1}^{N_{dis}} B\boldsymbol{v}_i^2 / bdl \tag{11}$$

where B is drag coefficient. According to Eq. 11, if one assumes a constant dislocation length during motion (such as in 2D DD simulation) and the influence of burst duration Δt_d is ignored, ΔE_d is roughly proportional to v^2. In Table III, absolute dislocation velocity V is used, ΔE_d is also roughly proportional to V^2. Using conservation of probability $P(\Delta E_d)d\Delta E_d = P(V)dV$, the power law exponent of dislocation velocity $m_V = 2m_E - 1$. If the mean field description of $\dot{\varepsilon}^p$ is valid and $\rho_m \Delta t_d$ does not change too much, $m_{ep} \approx 2m_E - 1$.

REFERENCES

* cuiyinan@ucla.edu

[1] M. C. Miguel, A. Vespignani, S. Zapperi, J. Weiss, and J. R. Grasso, Nature **410**, 667 (2001).
[2] D. M. Dimiduk, C. Woodward, R. LeSar, and M. D. Uchic, Science **312**, 1188 (2006).
[3] F. F. Csikor, C. Motz, D. Weygand, M. Zaiser, and S. Zapperi, Science **318**, 251 (2007).
[4] S. Papanikolaou, F. Bohn, R. L. Sommer, G. Durin, S. Zapperi, and J. P. Sethna, Nature Phys. **7**, 316 (2011).
[5] M. Zaiser, Journal of the Mechanical Behavior of Materials **22**, 89 (2013).
[6] J. Weiss, T. Richeton, F. Louchet, F. Chmelik, P. Dobron, D. Entemeyer, M. Lebyodkin, T. Lebedkina, C. Fressengeas, and R. J. McDonald, Phys. Rev. B **76**, 224110 (2007).
[7] K. Ng and A. Ngan, Acta Mater. **56**, 1712 (2008).
[8] A. Ngan and K. Ng, Philos. Mag. **90**, 1937 (2010).
[9] P. D. Ispánovity, I. Groma, G. Györgyi, F. F. Csikor, and D. Weygand, Phys. Rev. Lett. **105**, 085503 (2010).
[10] N. Friedman, A. T. Jennings, G. Tsekenis, J.-Y. Kim, M. Tao, J. T. Uhl, J. R. Greer, and K. A. Dahmen, Phys. Rev. Lett. **109**, 095507 (2012).
[11] J. Hu, Z. Liu, Y. Cui, Z. Wang, Z. Shan, and Z. Zhuang, Journal of Applied Mechanics **81**, 091007 (2014).
[12] H. Tang, K.W. Schwarz, and H.D. Espinosa, Physical review letters **100**, 185503 (2008).
[13] S. I. Rao, D. Dimiduk, T. A. Parthasarathy, M. Uchic, M. Tang, and C. Woodward, Acta Mater. **56**, 3245 (2008).
[14] Y. Cui, P. Lin, Z. Liu, and Z. Zhuang, Int. J. Plast. **55**, 279 (2014).
[15] Y.-n. Cui, Z.-l. Liu, and Z. Zhuang, J. Mech. Phys. Solids. **76**, 127 (2015).
[16] T. Crosby, G. Po, C. Erel, and N. Ghoniem, Acta Mater. **89**, 123 (2015).
[17] M. Zaiser and N. Nikitas, J. Stat. Mech.: Theory Exp. **2007**, P04013 (2007).
[18] R. Maass, M. Wraith, J.T. Uhl, J.R. Greer, K.A. Dahmen, Phys. Rev. E **91**, 042403 (2015).
[19] Y. Cui, G. Po, and N. Ghoniem, Physical Review Letters **117**, 155502 (2016).
[20] J. T. Uhl, S. Pathak, D. Schorlemmer, X. Liu, R. Swindeman, B. A. Brinkman, M. LeBlanc, G. Tsekenis, N. Friedman, R. Behringer, *et al.*, Sci. Rep. **5**, 16493 (2015).
[21] G. Po and N. Ghoniem, ⟨https://bitbucket.org/model/model/wiki/home⟩ (2015).
[22] N.M. Ghoniem, S.H. Tong, and L.Z. Sun, Phys. Rev. B **61**, 913 (2000).
[23] G. Po, M. Lazar, D. Seif, and N. Ghoniem, J. Mech. Phys. Solids. **68**, 161 (2014).
[24] G. Po, M. S. Mohamed, T. Crosby, C. Erel, A. El-Azab, and N. Ghoniem, JOM **66**, 2108 (2014).
[25] A. Lehtinen, G. Costantini, M. J. Alava, S. Zapperi, and L. Laurson, Physical Review B **94**, 064101 (2016).
[26] M. D. Uchic and D. M. Dimiduk, Mater. Sci. Eng. A **400**, 268 (2005).
[27] O. L. Warren, S. A. Downs, and T. J. Wyrobek, Zeitschrift für Metallkunde **95**, 287 (2004).
[28] X. Illa, P. Winkelmayer, and E. Vives, Physical Review B **92**, 184107 (2015).
[29] J. A. El-Awady, M. Wen, and N. M. Ghoniem, J. Mech. Phys. Solids. **57**, 32 (2009).
[30] Y. Cui, G. Po, and N. Ghoniem, Acta Materialia **108**, 128 (2016).
[31] Z. Shan, R. K. Mishra, S. S. Asif, O. L. Warren, and A. M. Minor, Nature Mater. **7**, 115 (2008).
[32] Z.-J. Wang, Q.-J. Li, Y.-N. Cui, Z.-L. Liu, E. Ma, J. Li, J. Sun, Z. Zhuang, M. Dao, Z.-W. Shan, S. Suresh, Proc. Natl. Acad. Sci. USA. **112**, 13502 (2015).
[33] Y.-n. Cui, Z.-l. Liu, Z.-j. Wang, and Z. Zhuang, J. Mech. Phys. Solids. **89**, 1 (2016).
[34] D. Dimiduk, M. Uchic, S. Rao, C. Woodward, and T. Parthasarathy, Modell. Simul. Mater. Sci. Eng. **15**, 135 (2007).
[35] Z.-J. Wang, Q.-J. Li, Z.-W. Shan, J. Li, J. Sun, and E. Ma, Applied Physics Letters **100**, 071906 (2012).
[36] C. Fressengeas, A.J. Beaudoin, D. Entemeyer, T. Lebedkina, M. Lebyodkin and V. Taupin, Phys. Rev. B **79**, 014108 (2009).
[37] P. Lin, Z. Liu, Y. Cui, and Z. Zhuang, Int. J. Solids Struct. **69**, 267 (2015).
[38] V. Navas-Portella, Á. Corral, and E. Vives, Physical Review E **94**, 033005 (2016).
[39] C. Scruby, H. Wadley, and J. Sinclair, Philos. Mag. A **44**, 249 (1981).
[40] T. Richeton, J. Weiss, and F. Louchet, Acta Mater. **53**, 4463 (2005).
[41] J. Weiss, F. Lahaie, and J. R. Grasso, J. Geophys. Res. **105**, 433 (2000).
[42] B. Devincre, T. Hoc, and L. Kubin, Science **320**, 1745 (2008).
[43] M. Zaiser, J. Schwerdtfeger, A. Schneider, C. Frick, B. G. Clark, P. Gruber, and E. Arzt, Philos. Mag. **88**, 3861 (2008).
[44] S. Brinckmann, J.-Y. Kim, and J. R. Greer, Phys. Rev. Lett. **100**, 155502 (2008).
[45] M. Lebyodkin, L. Dunin-Barkowskii, Y. Brechet, Y. Estrin, and L. Kubin, Acta Mater. **48**, 2529 (2000).
[46] T. Niiyama and T. Shimokawa, Phys. Rev. B **94**, 140102 (2016).
[47] T. Niiyama and T. Shimokawa, Physical Review E **91**, 022401 (2015).
[48] T. Richeton, P. Dobron, F. Chmelik, J. Weiss, and F. Louchet, Materials Science and Engineering: A **424**, 190 (2006).
[49] J. Weiss, W. B. Rhouma, T. Richeton, S. Dechanel, F. Louchet, and L. Truskinovsky, Phys. Rev. Lett. **114**, 105504 (2015).
[50] M. Zaiser and P. Moretti, Journal of Statistical Mechanics: Theory and Experiment **2005**, P08004 (2005).
[51] X. Zhang, B. Pan, and F. Shang, Europhys. Lett. **100**, 16005 (2012).
[52] S. Zapperi, A. Vespignani, and H. E. Stanley, Nature **388**, 658 (1997).

[53] F.-J. Pérez-Reche, L. Truskinovsky, and G. Zanzotto, Physical review letters **101**, 230601 (2008).
[54] A. Clauset, C. R. Shalizi, and M. E. Newman, SIAM Rev. **51**, 661 (2009).
[55] H. Bauke, Eur. Phys. J. B **58**, 167 (2007).